京都大学防災研究所年報 第 64 号 B
DPRI Annuals, No. 64 B, 2021

Wavelet Analysis of Thermal Activity and Cloud Initiation based on Boundary Layer Radar and Time Lapse Camera Observation

Ginaldi Ari NUGROHO(1), Kosei YAMAGUCHI,
Masayuki K. YAMAMOTO(2), Seiji KAWAMURA(2), and Eiichi NAKAKITA

(1) Graduate School of Engineering, Kyoto University, Kyoto, Japan.
(2) National Institute of Information and Communications Technology, Tokyo, Japan

Synopsis

This study aims at observing cumulus clouds generated in the boundary layer and to investigate relationship between the cumulus clouds and local thermals. Individual cumulus clouds generated in the boundary layer were observed by a time-lapse camera. Vertical air velocity measured by a Boundary Layer Radar (BLR) was used to observe local thermals. The BLR was collocated with the time-lapse camera. Wavelet coherence was used to quantify the relationship between the two variables. We found that an upward air motion was observed ahead of a cumulus cloud development below 900 m height within 27 events of an individual cumulus cloud. The phase classification showed that 40.7 % of the local thermal event in the boundary layer region impacted the cumulus cloud development. The scale period of these local thermals varied from 0.5 until 8 min.

Keywords: Wavelet, Phase classification, Thermal, Cumulus cloud.

1. Introduction

This study aims at observing the cumulus clouds generated in the boundary layer and to investigate relationship between the cumulus clouds and local thermals. Unlike the previous study by Klinger et al. (2017) that used numerical simulation, we used field observation data and the wavelet coherence method. Individual cumulus clouds generated at the top of the boundary Layer were measured by a time-lapse camera. Vertical air velocity measured by a Boundary Layer Radar (BLR) was used as a representation of the local thermal.

Wavelet coherence analysis is often used as a tool to find the relationship between two variables (Ng. Eric and Chan, 2012). This study uses wavelet coherence analysis to investigate the connection between local thermal and cumulus cloud development.

The conditions within the boundary layer affect cloud development. Boundary layer conditions which could signifincantly control the cumulus clouds development are the turbulent profiles, boundary layer depth and the updraft condition (Lareau et al., 2018). In this study, variables such as boundary layer height, updraft condition, and vertical velocity condition at the boundary layer height are also considered in the wavelet coherence analysis because they also relate to the boundary layter condition.

2. Data and Methodology

2.1 Data and Observation Location

Dataset used in this study is based on field experiment conducted in Kobe city, Japan. The experiment took place during the summer season (from July until September) in 2018 and 2020. We only focused on the daytime period from 5 am until 4 pm JST. The reason is that probability of thermal occurrence is high only during those periods.

BLR used in this study is equipped with range imaging and oversampling functions to enhance the vertical scale capability as small as 100 m (Yamamoto et al.,2014). Adaptive clutter suppression is also implemented to mitigate clutter contamination in received signals (Yamamoto et al., 2017). Echo power, vertical air velocity, and signal-to-noise ratio (SNR) were collected with a range sampling of 15 or 30 m intervals with a time interval of 8.192 s. This setting was used to resolve fine-scale perturbations of vertical air velocity in thermals.

Cloud images from three time-lapse cameras were utilized. The first camera is placed in the same location as the BLR. The camera points upward to capture the cloud above BLR. Two other cameras are installed 2.01 km away from the BLR location. The two cameras are placed on the rooftop on the edge of the building, with a distance of 76 m. The setting of this camera is pointing towards the BLR location to capture the cloud development vertically. Time synchronization among the three-camera was conducted using the NICT timestamp as the time reference. The frame rate is 10 frames per second (fps) with a 1920 x 1080 pixels resolution.

2.2 Cloud Pixel Area

The image captured from the first camera was cropped into 200 x 200 pixels using digimizer software. Digimizer is usually used in a study that needs image analysis (Tchorz-Trzeciakiewicz and Kłos, 2017).

Digimizer calculates the pixel area of the cloud image and then archives it with the image timestamp to create time series of individual cloud development events. Time series of each events was produced from a sequence of cloud pixel area in time. Figure 1 is an example of a time series dataset of the cloud pixel area.

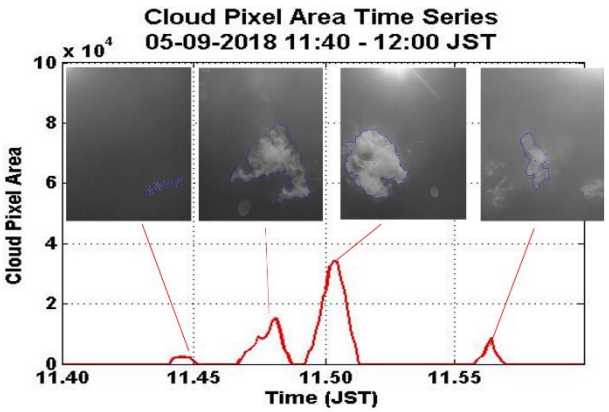

Fig. 1 Time series of cloud pixel area and cloud images from 11:40 – 12:00 JST on September 5 2018.

2.3 Local Thermal

Thermals were detected from the BLR vertical air velocity that extended along with the height. Vertical coverage of the BLR observation was limited only from 300 – 1700 m in the boundary layer region. Hampel filter was applied to eliminate outliers from the vertical air velocity data. Hampel filter detects an outlier and replaces it with the median within certain data window near the outlier location (Pearson et al., 2016).

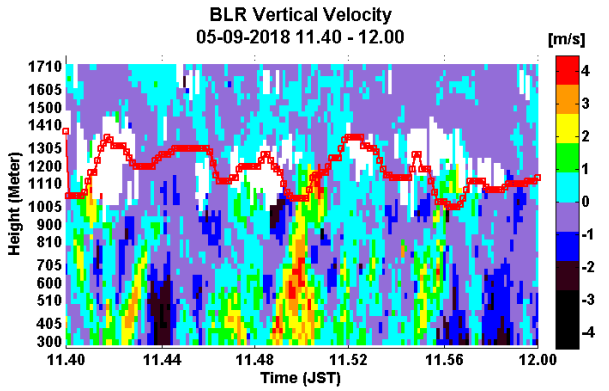

Fig. 2 Time altitude cross-section of vertical air velocity from 11:40 until 12:00 JST on September 5 2018. A positive value represents the upward movement. Red line is the BL height derived from the BLR echo power.

Boundary layer (BL) height was also estimated using the SNR measured by BLR. A method based on Angevine et al. (1994) was used to compute the BL height from the peak value of SNR in a certain period (24 s). Figure 2 is an example of local thermal events observed by BLR. The local thermal depicted by the continuous structures of the updraft (positive value). Meanwhile the BL height calculation is depicted in red line on Fig 2 to indicate the thermal location within the boundary layer.

2.4 Wavelet Coherence

Two time-series datasets (i.e., the cloud pixel area and the vertical air velocity) were used in the wavelet coherence analysis. In the first step, the two datasets were normalized to solve their difference in the unit. In the next step, the wavelet power spectrum for each dataset was calculated. Cross wavelet calculation using conjugation from two wavelet power spectrum was the third step. After that, wavelet phase coherence level and phase difference could be calculated using Equations (1) and (2) based on the wavelet power spectrum and cross wavelet result.

$$R^2(n,s) = \frac{[W^{xy}(n,s)]^2}{[W^x(n,s)]^2[W^y(n,s)]^2} \quad \ldots\ldots\ (1)$$

$$\Delta\varphi = \tan^{-1}\frac{\text{imaginary}(W^{xy})}{\text{real}(W^{xy})} \quad \ldots\ldots\ (2)$$

$R^2(n,s)$ is the phase coherence level (range from 0 to 1), and $\Delta\varphi$ is the phase difference that represent the phase relationship. W^x and W^y are the wavelet power spectrum of two-time series x(n) and y(n), respectively. W^{xy} is the cross wavelet between the two power spectrums. Meanwhile, s is the wavelet scale, and n is the time scale. The data processing described above is based on Grinsted et al. (2004). Morlet was used as the mother wavelet because it was suitable to detect the variations and the increase value of the cloud pixel area and the vertical air velocity. Classification of the phase relationship was conducted to simplify the relationship between the cloud pixel area and the vertical air velocity. The requirement for the classification is high phase coherence level and located outside the COI (cone of influence).

Four phased based on the relationships are defined in this study. Phase one is the in-phase coherence ($-\pi/4<\Delta\varphi<\pi/4$). This means that the phase difference of both time series (vertical air velocity and cloud pixel area) is almost zero or in phase (between -44° to 44°). Phase two is the anti-phase coherence ($\pi-\pi/4<\Delta\varphi<\pi+\pi/4$). This type of phase is categorized as a phase difference from 136° to 180° and -136° to -180° (to represent phase difference of more than 180°).

Phase three is the lagging phase coherence ($\pi/2-\pi/4<\Delta\varphi<\pi/2+\pi/4$). This type represents the condition where the phase difference is 45° to 135° (vertical air velocity time series have a delay between 45° to 135° compared with cloud pixel area time series). In this condition could also mention as the vertical air velocity lagging to cloud pixel area. Phase four is the leading coherence ($-\pi/2-\pi/4<\Delta\varphi<-\pi/2+\pi/4$). In this condition, the phase difference between vertical air velocity time series and cloud pixel area is -135° to -45°. This condition could be mention as the vertical air velocity is leading with cloud pixel area time series by phase difference of -135° to -45°.

The four-phase classification is represented in the wavelet coherence result with the colors as follows: in-phase coherence (cyan), anti-phase coherence (blue), leading phase (yellow), and lagging phase (green). Classification results are later shown in Fig.4 and 6.

Since the goal of this study is to find relationship where local thermal impacts cumulus cloud generation, leading phase (phase four) is the aim that we would like to search in this study. Leading phase in this study is defined as the phase when the rise of the positive vertical air velocity (updraft) occurs first before the rise of the cloud pixel area (updraft leading cloud pixel area occurrence).

3. Result and Discussion

In this study, 14 time-series datasets were used. Within

these 14 datasets, there are 40 events of cumulus cloud captured by the time-lapse cameras along with the vertical air velocity observe by BLR. These events were supplied to the wavelet coherence, in which the cloud pixel area was compared with the vertical air velocity every heigh. Figure 3 is an example of wavelet coherence at 600 and 900 m height from 11:40 JST to 11:50 JST on September 5, 2018.

Figs. 3a and 3c show the normalized time series comparison of the camera cloud pixel and BLR vertical air velocity at the height of 600 m and 900 m, respectively. The wavelet coherence in Figs. 3b and 3d show the coherence level between the two time-series data. Results of the wavelet phase coherence and phase difference is used to determine the phase classification.

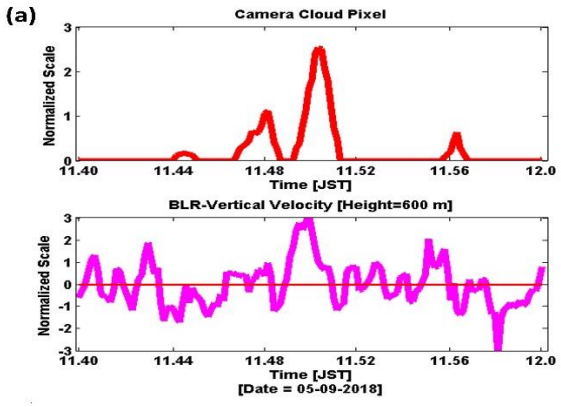

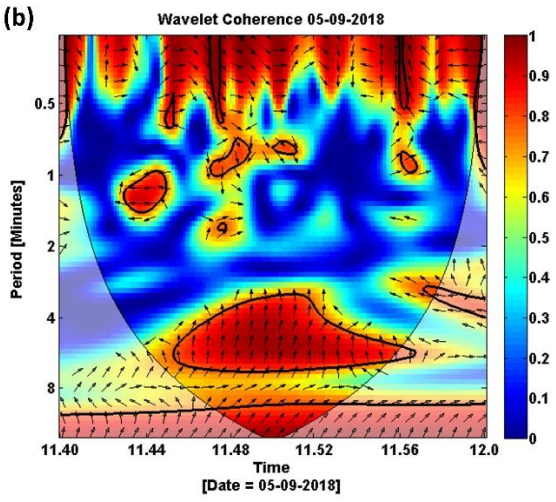

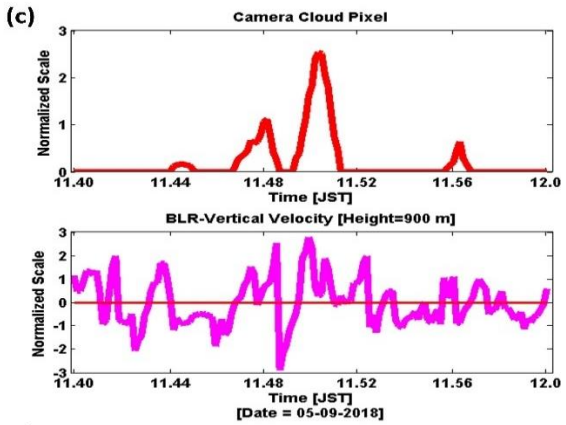

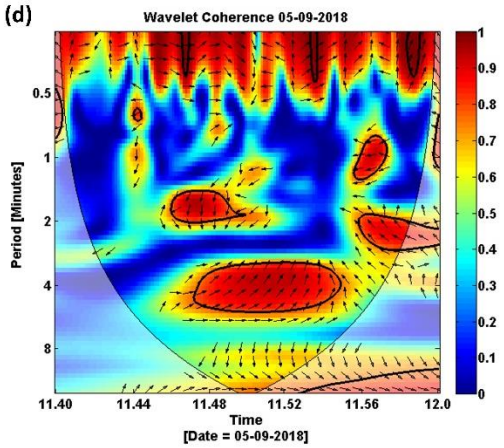

(d)

Fig. 3 Wavelet coherence result from 11:40 to 11:58 JST on September 5 2018. (a) Time series of the cloud pixel area and that of the vertical air velocity at 600 m height. (b) Wavelet coherence result of the two time series shown in (a). (c) Same as (a) except that the vertical air velocity at 900 m height is shown. (d) Wavelet coherence result of the two time series shown in (c). In (b) and (d), the x-axis represents time, and the y-axis represents wavelet scale period. Colored contour show the coherence level. The phase of the coherence is denoted by the arrow with anticlockwise rotation.

Calculation results with high phase coherence level and located outside of COI (as marked in the thick black region in Fig 3b and Fig 3d) were used in the phase classification. Figs. 4a and 4d are examples of phase classification for the phase coherence results shown in Figs. 3b and 3d. The average was computed along the y

axis. These averaged results represent the phase classification in one single height and depicted in Fig 4b and Fig 4e. Meanwhile, average calculations along the x-axis are depicted in Figs. 4c and 4f. These results represent the phase classification based on the scale period. Furthermore, the averaging process along the x and y axis were applied to every height from 300 m until 1700 m.

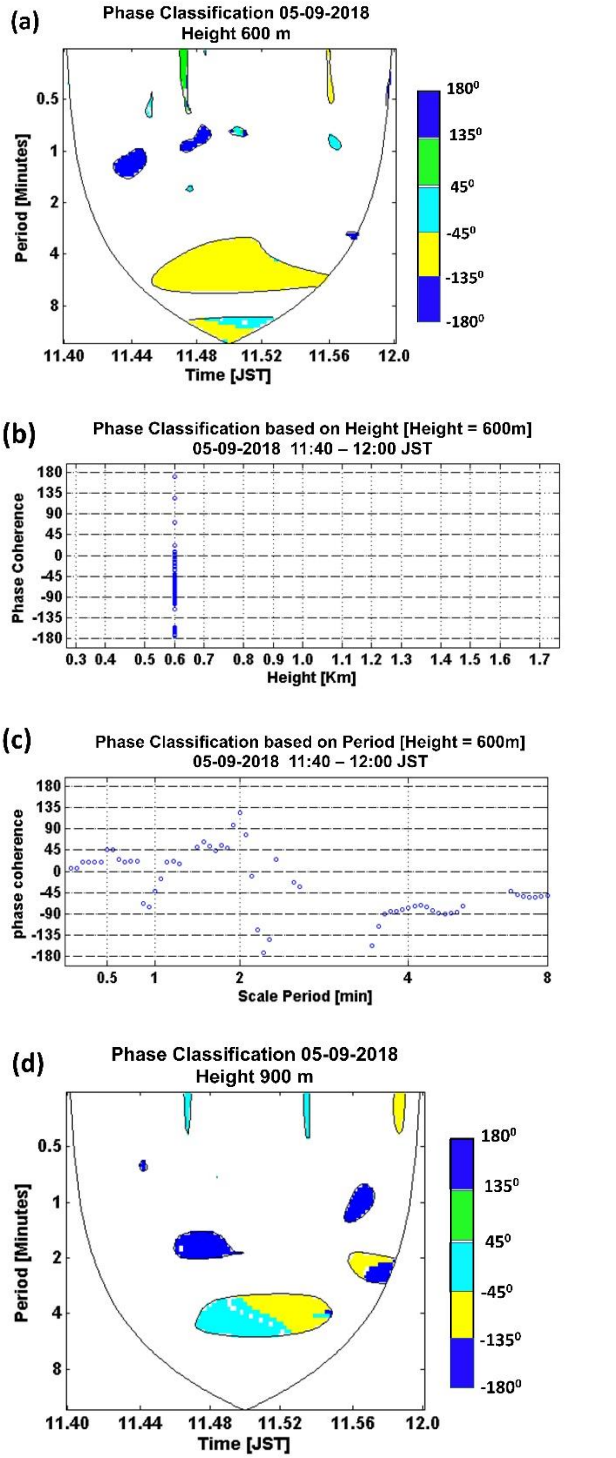

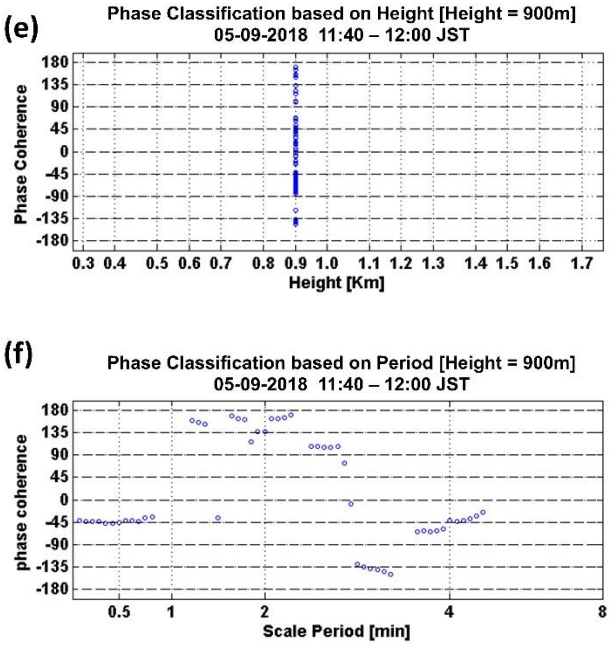

Fig. 4 Results of phase classification for the wavelet coherence results shown in Fig. 3. (a) Phase classification at 600 m height. (b) Phase classification after averaging along the scale period at 600 m height. (c) Phase classification after averaging along time at 600 m, (d)-(f) Same as (a)-(c) expect that results at 900 m height are shown.

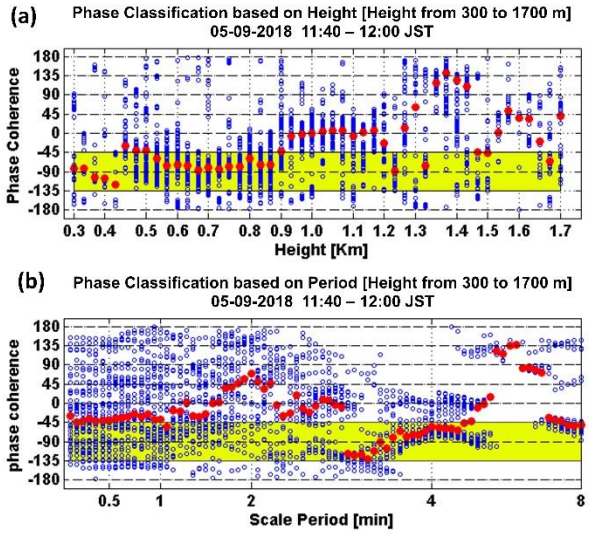

Fig. 5 Example of phase classification in the same period as shown in Fig. 3: (a) Phase classification after averaging along the scale period. (b) Phase classification after averaging along time. Red marker represents medians. The yellow area has the leading phase ($-\pi/2-\pi/4<\Delta\varphi<-\pi/2+\pi/4$ or -45° until -135°).

Figure 5 is calculation results from 300 m until 1700 m height. In order to find the distinct pattern, medians were also plotted. In Fig. 5a, continuous leading phases were found.

All of the 14 datasets were calculated to analyze the continuous leading phase. When the averaging along the scale period was executed (i.e., the averaging was carried out based on height), there were only 10 datasets that had continuous leading phase. In the 10 datasets, 9 datasets were collected below 900 m height. When the averaging was executed along time (i.e., based on the scale period, mainly the consistent leading phase is located at the scale period from 2 until 8 min. Table 1 is the selected 9 datasets along with the time and number of events. In total, 27 events were observed.

Table 1. The chosen dataset with leading phase.

No	Date	Time	Number of events
1	20180905	11:40-12:00	4
2	20200812	09:32-09:50	3
3	20200812	11:10-11:49	4
4	20200812	12:10-12:20	2
5	20200814	09:50-10:29	4
6	20200814	10:42-10:58	2
7	20200814	11:32-11:48	1
8	20200814	12:30-12:46	2
9	20200815	08:20-08:44	5

Further investigation is conducted to observe whether or not this continuous leading phase is related to the boundary layer condition. Cloud pixel area is then calculated using wavelet coherence with three different variables: 1) boundary layer height (hereafter variable A), 2) vertical air velocity at the BL height as a representation of the boundary layer condition (hereafter variable B), 3) updraft averaged from height 300 m until boundary layer height (hereafter variable C). Figure 6 is an example of a wavelet result based on three variables.

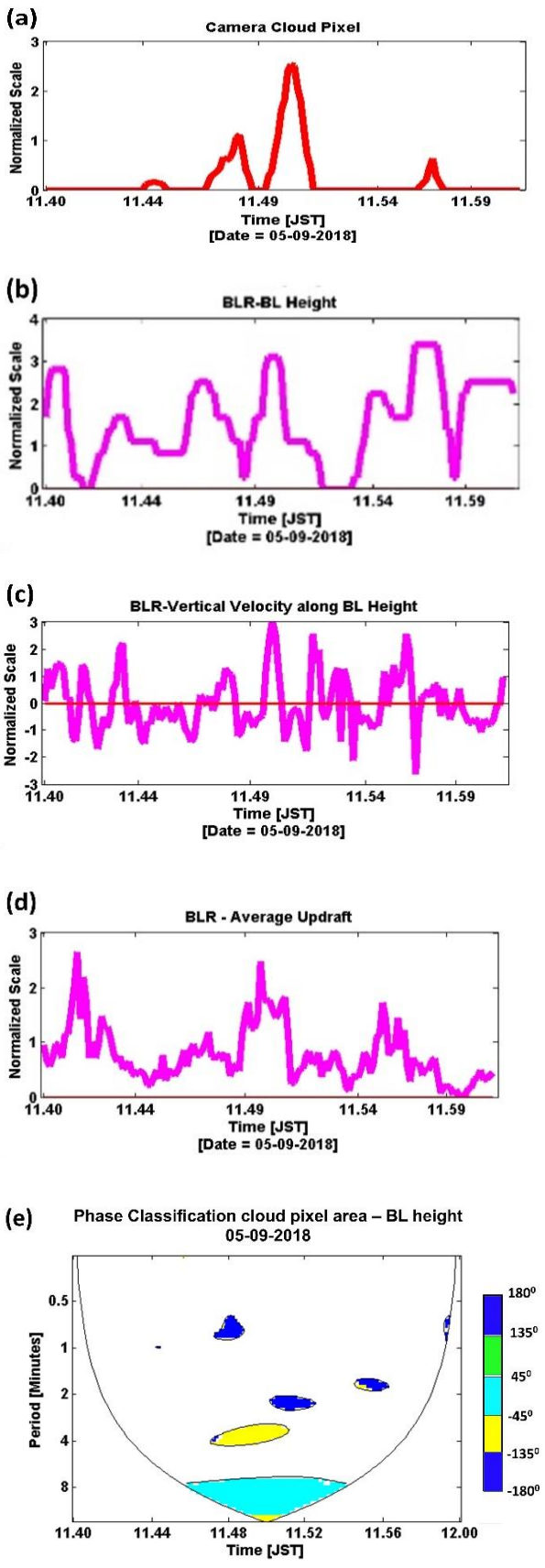

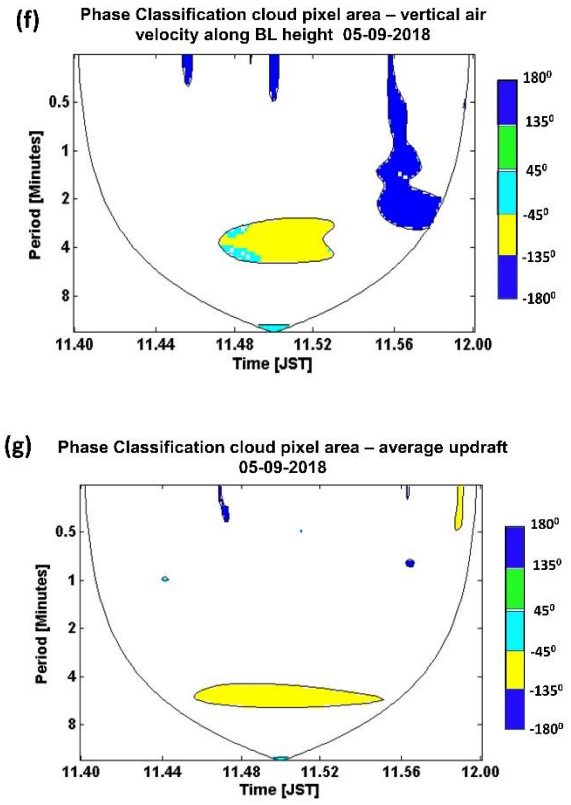

Fig. 6 Example of a wavelet coherence from 11:40 to 11:58 JST on September 5 2018, with phase classification between time series of camera cloud pixel and three different variables. Time series of (a) Cloud pixel area, (b) BL height, (c) Vertical air velocity along with BL height, and (d) Averaged updraft. Coherence wavelet result for (e) the BL height, (f) vertical air velocity along the BL height, and (g) the averaged updraft.

Visual inspection was made to find the start time of each event. Results of phase relationship and the scale period is depicted in Table 2. The highest occurrence of leading phase was found in the results for variables B and C (11 events out of 27 events). The percentage of the occurrence is 40.7%. These results shows almost half of the cloud pixel area events within the 9 datasets related to updraft at the boundary layer heights. The scale period of the leading phase is varied from 0.5 until 8 min. This result supports the previous research by Klinger et al. (2017) that local thermal has a big part in developing cumulus clouds. On the other hand, the other two time-lapse cameras observed that the cumulus clouds did not develop well to penetrate into the free atmosphere. Meanwhile, concerning the impact of boundary layer depth, the highest occurrence using variable A is the lagging phase (13 events from a total of 27 events or 48 %). This result showed that the increase of the BL height follows the cloud pixel area existence. Leading phase only contributes fewer events, which could not give any potential proof that the increase of BL height has a significant impact on the development of cumulus clouds.

4. Conclusion

This study described the ability of wavelet coherence analysis to investigate the relationship between cumulus cloud development and local thermals. In this study, cloud pixel area was used as a representation of cumulus cloud development, and vertical air velocity was used as a representation of local thermal. The phase classifications were used to quantify the relationship between them. The first goal is finding the leading phase which indicates that updraft is followed by cumulus cloud development. The results showed that there were 9 datasets out of 14 datasets that had a continuous leading phase below 900 m height. The second goal is finding the relationship between cloud pixel area and three variables (BL height, vertical air velocity at the BL height, and updraft averaged from height 300 m until boundary layer height) in the 9 datasets with the leading phase of the upward motion. The result showed that almost half of the cloud pixel area events relate to the averaged updraft at the boundary layer heights. Meanwhile, results of wavelet coherent analysis were not significant to prove that the boundary layer height impacts the cumulus cloud development.

Acknowledgments

This work was supported by JSPS KAKENHI, Grant Numbers 15H05765, 20H02258, 16K12861.

Table 2. Collected phase relationship and scale period.

Event	Date	Start time	BL height		Vertical velocity at BL height		Average Updraft	
			phase	scale period	phase	scale period	phase	scale period
1	20180905	11:44:19	x	x	x	x	lagging	1
2	20180905	11:46:49	leading	4	leading	4	leading	4
			lagging	8				
3	20180905	11:49:29	leading	4	leading	4	leading	4
			lagging	8				
4	20180905	11:55:54	x	x	x	x	anti-phase	0.05
5	20200812	09:35:36	lagging	0.5_1	x	x	lagging	2_4
6	20200812	09:41:36	lagging	0.5_1	x	x	leading	4
7	20200812	09:44:36	lagging	0.5_1	leading	4	leading	4
8	20200812	11:16:26	x	x	x	x	leading	1_2
9	20200812	11:25:36	leading	4	lagging	8	lagging	0.5_1
10	20200812	11:36:56	anti-phase	2_4	lagging	8	leading	8
11	20200812	11:43:36	x	x	lagging	2_4	X	x
12	20200812	12:13:15	lagging	2_4	leading	2_4	anti-phase	1_2
							lagging	8
13	20200812	12:16:15	lagging	8	lagging	8	lagging	8
14	20200814	09:53:45	x	x	anti-phase	1_2	lagging	4_8
15	20200814	09:59:21	lagging	1_2	lagging	8	leading	4_8
16	20200814	10:09:19	x	x	leading	2_4	X	x
17	20200814	10:18:27	lagging	0.5	lagging	4	anti-phase	0.5_1
18	20200814	10:44:08	leading	0.5_1	x	x	X	x
19	20200814	10:53:49	lagging	2_4	leading	4_8	X	x
20	20200814	11:39:25	lagging	0.5_1	leading	0.5_1	leading	0.5
21	20200814	12:32:40	anti-phase	0.5_1	x	x	leading	2_4
22	20200814	12:42:14	anti-phase	1_2	leading	0.5	anti-phase	2_4
23	20200815	08:22:09	anti-phase	1_2	lagging	1_2	anti-phase	1
24	20200815	08:25:16	lagging	2	leading	0.5	anti-phase	2_4
			anti-phase	0.5				
25	20200815	08:29:36	anti-phase	0.5_1	leading	0.5_1	leading	1_2
26	20200815	08:32:15	lagging	0.5_1	lagging	0.5	X	x
27	20200815	08:39:16	leading	2_4	leading	0.5	leading	0.5_1
							anti-phase	2

References

Angevine, W.M., White, A.B., and Avery, S.K. (1994): Boundary-layer depth and entrainment zone characterization with a boundary-layer profiler, Boundary-Layer Meteorology, Vol. 68, No. 4, pp. 375-385.

Ng, Eric. K. and Chan, J.C. (2012): Geophysical applications of partial wavelet coherence and multiple wavelet coherence. Journal of Atmospheric and Oceanic Technology, Vol. 29, No. 12, pp. 1845-1853.

Grinsted, A., Moore, J.C., and Jevrejeva, S. (2004): Application of the cross wavelet transform and wavelet coherence to geophysical time series, Nonlin. Processes Geophys, Vol. 11, pp. 561–566.

Klinger, C., Mayer, B., Jakub, F., Zinner, T., Park, S. B., and Gentine, P. (2017): Effects of 3-D thermal radiation on the development of a shallow cumulus cloud field. Atmospheric Chemistry and Physics, Vol. 17, No. 8, pp. 5477-5500.

Lareau, N.P., Zhang, Y., and Klein, S.A. (2018): Observed boundary layer controls on shallow cumulus at the ARM Southern Great Plains site. Journal of the Atmospheric Sciences, Vol. 75, No. 7, pp. 2235-2255.

Pearson, R.K., Neuvo, Y., Astola, J. and Gabbouj, M. (2016): Generalized hampel filters. EURASIP Journal on Advances in Signal Processing, No. 1, pp. 1-18.

Torrence. C. and Campo, G.P. (1998): A Practical Guide to Wavelet Analysis. Bulletin of the American Meteorological Society, Vol. 79, pp. 61-78.

Tchorz-Trzeciakiewicz, D.E. and Kłos, M. (2017). Factors affecting atmospheric radon concentration, human health. Science of the total environment, Vol. 584, pp. 911-920.

Yamamoto, M.K., Fujita, T., Aziz, N.H.B.A., Gan, T., Hashiguchi, H., Yu, T.Y. and Yamamoto, M. (2014): Development of a digital receiver for range imaging atmospheric radar. J. Atmos. Sol.-Terr. Phys, Vol. 118, pp. 35-44.

Yamamoto, M.K., Kawamura, S. and Nishimura, K. (2017): Facility implementation of adaptive clutter suppression to an existing wind profiler radar: First result. IEICE Communications Express, Vol. 6, No. 9, pp. 513-518.

(Received August 31, 2021)